

Infrared 3–4 μm Spectroscopy of Nearby PG QSOs and AGN–Nuclear Starburst Connections in High-luminosity AGN Populations

Masatoshi IMANISHI^{1,2}

Subaru Telescope, 650 North A’ohoku Place, Hilo, Hawaii, 96720, U.S.A.

masa.imanishi@nao.ac.jp

Kohei ICHIKAWA, Tomoe TAKEUCHI

Department of Astronomy, Kyoto University, Kyoto 606-8502, Japan

Nozomu KAWAKATU

Department of Physics, University of Tsukuba, Tennodai, Tsukuba 305-8577, Japan

Nagisa OI^{2,3}, and Keisuke IMASE^{2,3}

Department of Astronomy, School of Science, Graduate University for Advanced Studies (SOKENDAI), Mitaka, Tokyo 181-8588, Japan

¹*Department of Astronomy, School of Science, Graduate University for Advanced Studies (SOKENDAI), Mitaka, Tokyo 181-8588, Japan*

²*National Astronomical Observatory, 2-21-1, Osawa, Mitaka, Tokyo 181-8588, Japan*

³*Subaru Telescope, 650 North A’ohoku Place, Hilo, Hawaii, 96720, U.S.A.*

(Received ; accepted)

Abstract

We present the results of infrared *L*-band (3–4 μm) slit spectroscopy of 30 PG QSOs at $z < 0.17$, the representative sample of local high-luminosity, optically selected AGNs. The 3.3 μm polycyclic aromatic hydrocarbon (PAH) emission feature is used to probe nuclear (<a few kpc) starburst activity and to investigate the connections between AGNs and nuclear starbursts in PG QSOs. The 3.3 μm PAH emission is detected in the individual spectra of 5/30 of the observed PG QSOs. We construct a composite spectrum of PAH-undetected PG QSOs and discern the presence of the 3.3 μm PAH emission therein. We estimate the nuclear-starburst and AGN luminosities from the observed 3.3 μm PAH emission and 3.35 μm continuum luminosities, respectively, and find that the nuclear-starburst-to-AGN luminosity ratios in PG QSOs are similar to those of previously studied AGN populations with lower luminosities, suggesting that AGN–nuclear starburst connections are valid over the wide luminosity range of AGNs in the local universe. The observed nuclear-starburst-to-AGN luminosity ratios in PG QSOs with available supermassive black hole masses are comparable to a theoretical prediction based on the assumption that the growth of a supermassive black hole is controlled by starburst-induced turbulence.

Key words: galaxies: active — galaxies: nuclei — quasars: general — galaxies: starburst — infrared: galaxies

1. Introduction

The apparent ubiquity of supermassive black holes (SMBHs) in the spheroidal components of present-day galaxies and the correlation between the masses of SMBHs and spheroidal stars (Magorrian et al. 1998; Ferrarese & Merritt 2000) indicate that active galactic nucleus (AGN; SMBH-driven activity) and starburst activity are closely coupled. Theories also predict that starburst activity in the nuclear region of a galaxy can have a strong effect on a central AGN by regulating the mass accretion rate of a central SMBH (Norman & Scoville 1988; von Linden et al. 1993; Umemura et al. 1997; Umemura et al. 1998; Ohsuga et al. 1999; Wada & Norman 2002; Kawakatu et al. 2003; Vollmer & Beckert 2003; Kawakatu & Wada 2008; Collin & Zahn 2008; Wada et al. 2009). Hence, it is important to observationally ascertain whether, in what types of galaxies, and on which physical scale AGN and starburst activity are related.

To disentangle AGN and starburst activity in galaxies, it is essential to use an indicator that can trace *only* starburst or AGN activity. An effective tool for detecting starburst activity is the polycyclic aromatic hydrocarbon (PAH) emission features found in the infrared 3–20 μm wavelength range (Tielens 2008). In a starburst galaxy, PAHs in the photo-dissociation regions are excited without destruction by far-UV photons from stars, and so a starburst galaxy usually exhibits strong PAH emission features (Moorwood 1986; Roche et al. 1991; Genzel et al. 1998; Imanishi & Dudley 2000). However, in the near vicinity of an AGN, PAHs are destroyed due to strong X-ray radiation emanating from the AGN (Voit 1992). In the obscuring material surrounding a central AGN, PAH molecules at some distance from the AGN could be adequately shielded from such X-ray emission by gas and dust and could survive. However, no PAH-exciting UV photons from the AGN are available there, as the extinction rate is greater in the UV range than in the X-ray range, and

thus, PAH emission is absent from a pure AGN. If PAH emission is detected in a galaxy hosting an AGN, PAH-exciting UV photons from local energy sources (i.e., starbursts) are required. Thus, PAH emission is a very useful tool for detecting only starburst activity and investigating its properties by removing the contamination from an AGN, even in an AGN/starburst composite galaxy. More importantly, since dust extinction is small at $\lambda > 3 \mu\text{m}$ ($< 0.05 \times A_V$; Nishiyama et al. 2008; 2009), the absolute magnitude of modestly-obscured ($A_V < 20 \text{ mag}$) starburst activity is reasonably quantifiable from the *observed* (extinction-*uncorrected*) PAH emission luminosity (Mouri et al. 1990; Imanishi 2002; Soifer et al. 2002; Peeters et al. 2004; Smith et al. 2007). For these reasons, infrared 3–20 μm spectroscopy can be very effective for directly ascertaining AGN–starburst connections in galaxies in a quantitatively reliable manner.

Using the PAH emission features detected in the space-based Spitzer IRS observations (Houck et al. 2004), AGN–starburst connections in optically identified AGNs have been widely investigated (Schweitzer et al. 2006; Shi et al. 2007; Watabe et al. 2008; Watabe et al. 2009; Wu et al. 2009; Veilleux et al. 2009; Baum et al. 2010). However, the large aperture of the Spitzer IRS ($> 3''.6$) probes not only nuclear ($< \text{a few kpc}$) starbursts, but also spatially extended ($> \text{several kpc}$) star-forming regions in host galaxies. Although spatially extended star formation may be more quiescent than nuclear starbursts, it can dominate the total PAH emission flux in large-aperture spectroscopy because of its large surface area. With regard to possible connections between AGNs and starbursts, however, it is likely that *nuclear* starbursts have a stronger influence on an AGN due to the proximity to a central SMBH. The greater importance of *nuclear* starbursts (rather than spatially extended star-formation) to central AGNs was actually argued from observations (Watabe et al. 2008), suggesting that it is important to observationally investigate the relationship between *nuclear* starbursts and AGNs.

Ground-based, narrow-slit ($\sim 1''$) spectroscopy is better suited to detecting exclusively *nuclear* ($< \text{a few kpc}$) starbursts by reducing the contamination from spatially extended ($> \text{several kpc}$), quiescent star-forming activity in host galaxies. The 3.3 μm PAH emission feature is particularly useful for probing exclusively nuclear starbursts via ground-based slit spectroscopy, as it is in an appropriate wavelength range for terrestrial atmospheric transmission (i.e., *L*-band; 2.8–4.2 μm). Although a strong 11.3 μm PAH emission feature is also observable from the ground, the Earth’s atmospheric background level in the *N*-band (8–13 μm) is much higher than that in the *L*-band, making it more difficult to obtain spectra with sufficient S/N ratios around the 11.3 μm PAH emission.

Using the 3.3 μm PAH emission features detected in ground-based, narrow-slit spectra, the relationship between AGNs and *nuclear* starbursts was observationally investigated in the nearby Seyfert galaxies (a moderate-luminosity AGN population), and a positive luminosity correlation was found (Imanishi 2002; Imanishi 2003; Rodríguez-Ardila & Viegas 2003; Imanishi & Wada 2004).

Oi et al. (2010) has extended these results to low-luminosity AGNs and has confirmed that a similar correlation is valid in this case. It would be interesting to know if the AGN–nuclear-starburst connection holds in a high-luminosity AGN population, as theoretical predictions about AGN–nuclear-starburst connections are varied, and are sometimes contradictory. For example, Kawakatu & Wada (2008) predicted that the nuclear-starburst-to-AGN luminosity ratio will increase with increasing AGN luminosity, whereas Ballantyne (2008) has argued the contrary. Observations of high-luminosity AGNs are needed to resolve this issue.

In this paper, we present the results of ground-based, narrow-slit spectroscopy of PG QSOs (Schmidt & Green 1983), a higher-luminosity AGN population than the Seyfert galaxies in the local universe. Throughout this paper, $H_0 = 75 \text{ km s}^{-1} \text{ Mpc}^{-1}$, $\Omega_M = 0.3$, and $\Omega_\Lambda = 0.7$ are adopted to be consistent with our previous publications.

2. Targets

Target objects were selected from the PG QSO sample compiled by Schmidt & Green (1983), which is the representative high-luminosity, optically selected, type 1 unobscured AGN population in the local universe. Sources with $M_B < -23 \text{ mag}$, conventionally classified as QSOs (Schmidt & Green 1983), are the objects of particular interest for investigating AGN–nuclear-starburst connections in the high-luminosity AGN range. For the redshifted 3.3 μm PAH emission to be observable at a wavelength appropriate for terrestrial atmospheric transmission (i.e., *L*-band; 2.8–4.2 μm), we limit the redshifts of the target objects to less than 0.17. We divide the objects according to whether $M_B < -24.1 \text{ mag}$ or $-24.1 \leq M_B < -23 \text{ mag}$ (in the cosmology of Schmidt & Green, 1983), and refer to these two classes as high- and low-luminosity PG QSOs, respectively. The number of low-luminosity PG QSOs is larger than the number of high-luminosity PG QSOs.

For the high-luminosity PG QSOs, we set a declination limit of $-15^\circ \sim +65^\circ$ to facilitate observation with small airmass at Mauna Kea, Hawaii (our observation site). This selection resulted in ten high-luminosity PG QSOs at $z < 0.17$ (Table 1), all of which were observed.

Because the number of low-luminosity PG QSOs is larger, a more stringent declination limit of $-15^\circ \sim +55^\circ$ was imposed. Twenty low-luminosity PG QSOs remained (Table 1), and all were observed.

Our sample is statistically complete, and hence is useful for investigating general properties without any obvious selection bias. The redshift range is 0.061–0.167, where $1''$ corresponds to the physical scale of 1.1–2.7 kpc.

3. Observations and Data Reduction

We used the IRCS infrared spectrograph (Kobayashi et al. 2000) at the Nasmyth focus of the Subaru telescope (Iye et al. 2004) to obtain the new infrared *L*-band spectra

of the PG QSOs, with the exception of Mrk 1014, 3C 273, and I Zw 1, for which the IRTF telescope was used. Table 1 lists the observational details.

During the Subaru IRCS observations, the sky was clear. The seeing size in the K -band ($\lambda = 2.2 \mu\text{m}$), obtained from images taken prior to the L -band spectroscopy, was $0''.4$ – $0''.8$ in FWHM. The $0''.9$ -wide slit and L -grism were used with a 52-mas-pixel scale. The achievable spectral resolution was $R \sim 140$ at $\lambda \sim 3.5 \mu\text{m}$. The precipitable water was very low, 1–2 mm for the 2006 July and 2010 April observational runs, and <1 mm for the 2007 January run. We adopted a standard telescope nodding technique (ABBA pattern) with a throw of $7''$ along the slit to subtract background emission. We used the optical guider of the Subaru telescope to monitor the telescope tracking. The exposure time was 1.0–1.8 sec, and 30–60 coadds were employed at each nod position.

The IRCS was moved from the Cassegrain to the Nasmyth focus of the Subaru telescope in 2005. Afterward, the background level was high in the L -band because of the high emissivity of the Nasmyth image rotator. In 2008, the image rotator was recoated, and the resulting low background level enabled a higher achievable sensitivity in the 2010 April data than in the 2006–2007 data. Hence, for objects of the same apparent magnitude observed with the same exposure time, the data quality of the 2010 spectra is generally superior to that of the 2006–2007 spectra.

For all observational runs, F- or G-type main sequence stars (Table 1) were observed as standard stars, with a mean airmass difference of <0.1 compared with the individual PG QSOs, to correct for terrestrial atmospheric transmission and provide flux calibration. The L -band magnitudes of the standard stars were estimated from their V -band ($\lambda = 0.6 \mu\text{m}$) magnitudes, adopting the $V - L$ colors appropriate for the stellar types of the individual standard stars (Tokunaga 2000).

Standard data analysis procedures were employed using IRAF¹. Initially, frames taken with an A (or B) beam were subtracted from frames subsequently taken with a B (or A) beam, and the resulting subtracted frames were added and divided by a spectroscopic flat image. Bad pixels and pixels impacted by cosmic rays were then replaced with the interpolated values of the surrounding pixels. Finally, the spectra of the PG QSOs and the standard stars were extracted. The wavelength calibration was based on wavelength-dependent terrestrial atmospheric transmission. The spectra of the PG QSOs were divided by the observed spectra of the standard stars and were multiplied by the spectra of blackbodies with temperatures appropriate to the individual standard stars (Table 1).

The flux calibration was based on the signals from the PG QSOs and the standard stars detected inside our slit spectra. Seeing sizes in the K -band (and L -band) were al-

ways smaller than the employed slit widths, and the tracking performance of the Subaru telescope was already established. We thus expected that the possible slit loss for the compact emission would be insignificant. To reduce the scatter of the spectra, appropriate binning of spectral elements was performed, particularly for faint sources.

Mrk 1014 and I Zw 1 were observed with the IRTF SpeX (Rayner et al. 2003), and 3C 273 was observed with the IRTF NSFCAM (Shure et al. 1994). The details of the Mrk 1014 and 3C 273 observations are found in Imanishi et al. (2006). For I Zw 1, the observational details and data reduction were carried out in the same way as with Seyfert galaxies observed during the same period (2003 September) (Imanishi & Wada 2004). In summary, the $1''.6$ -wide slit and the 1.9 – $4.2 \mu\text{m}$ cross-dispersed mode of the SpeX were employed. The effective spectral resolution was $R \sim 500$.

4. Results

Figures 1 and 2 display the respective infrared 3.4 – $3.9 \mu\text{m}$ spectra of the high- and low-luminosity PG QSOs. The spectra of Mrk 1014 and 3C 273 were originally published in Imanishi et al. (2006), and are reproduced here. In all sources, the redshifted $3.3 \mu\text{m}$ PAH emission is within the 3.4 – $3.9 \mu\text{m}$ wavelength range in the observed frame (λ_{obs}). Only the spectra in the range $\lambda_{\text{obs}} = 3.4$ – $3.9 \mu\text{m}$ are shown, as (1) the data for $\lambda_{\text{obs}} < 3.4 \mu\text{m}$ generally exhibit large scatter due to the strong wavelength dependency of terrestrial atmospheric transmission, and (2) the data for $\lambda_{\text{obs}} > 3.9 \mu\text{m}$ are noisier owing to the increased terrestrial atmospheric background emission. This treatment is necessary to better visualize the possible signatures of weak $3.3 \mu\text{m}$ PAH emission features in PG QSOs.

Photometry at $3.7 \mu\text{m}$ with a $5''$ – $5''.5$ aperture can be found in the literature for many of the observed PG QSOs (Neugebauer et al. 1987; Sanders et al. 1989), and our flux estimates roughly agree with the photometric flux measurements in most cases, suggesting that (1) the infrared 3 – $4 \mu\text{m}$ emission is dominated by a spatially-compact component, and (2) the slit loss in our slit spectra is generally insignificant.

Unlike the Seyfert galaxies, which contain both type 1 unobscured and type 2 obscured AGNs (Huchra & Burg 1992; Spinoglio & Malkan 1989), the high-luminosity AGN sample is well established only for type 1 unobscured AGNs (Schmidt & Green 1983). For PG QSOs (=type 1 unobscured AGNs), the unattenuated featureless continuum emission originating from an AGN reduces the equivalent width of the $3.3 \mu\text{m}$ PAH emission originating from a starburst. Consequently, even for the PG QSOs with $3.3 \mu\text{m}$ PAH emission signatures, the PAH flux excess above the continuum level is small, making it difficult to trace the $3.3 \mu\text{m}$ PAH emission profile in detail. We thus assume a typical profile for the $3.3 \mu\text{m}$ PAH emission feature (Tokunaga et al. 1991). Table 2 summarizes the flux ($f_{3.3\text{PAH}}$), luminosity ($L_{3.3\text{PAH}}$), and rest-frame equivalent width ($\text{EW}_{3.3\text{PAH}}$) of the $3.3 \mu\text{m}$ PAH emission for the five PAH-detected PG QSOs.

¹ IRAF is distributed by the National Optical Astronomy Observatories, operated by the Association of Universities for Research in Astronomy, Inc. (AURA), under cooperative agreement with the National Science Foundation.

For comparison with $3.3\ \mu\text{m}$ PAH-derived starburst magnitudes, AGN luminosities are estimated from the continuum emission at $\lambda_{\text{rest}} = 3.35\ \mu\text{m}$. Given that the rest-frame equivalent width of the $3.3\ \mu\text{m}$ PAH emission feature (Table 2) is more than an order of magnitude lower than that of a pure starburst-dominated galaxy ($\sim 100\ \text{nm}$; Moorwood 1986; Imanishi & Dudley 2000), it is reasonable to assume that the observed $\lambda_{\text{rest}} = 3.35\ \mu\text{m}$ continuum emission of PG QSOs originates predominantly from AGNs. Table 3 lists the AGN continuum luminosities (λL_{λ}), and Figure 3(a) shows a histogram of the luminosities. The AGN continuum luminosity traces hot dust emission heated by the AGN at the inner part of the putative dusty torus (Antonucci & Millar 1985; Barvainis 1987).

Our spectra include important information on the continuum slopes of high-luminosity, type 1 unobscured AGNs. We estimate the continuum slope Γ ($F_{\lambda} \propto \lambda^{\Gamma}$) from data points in the range $\lambda_{\text{rest}} = 3.4\text{--}3.9\ \mu\text{m}$, as summarized in Table 3. The histogram of the Γ values is shown in Figure 3(b). A larger Γ value means a redder continuum. The Γ values are in the range $-1.2 \sim -0.2$, except for PG 0052+251 and PG 1202+281. The median Γ value is -0.8 , which is larger (redder) than for starburst-dominated galaxies ($\Gamma = -2$; $F_{\lambda} \propto \lambda^{\Gamma}$; Imanishi et al. 2010).

5. Discussion

5.1. AGN - nuclear starburst connections in PG QSOs

The detection rate of the $3.3\ \mu\text{m}$ PAH emission feature is only 17% ($= 5/30$) for PG QSOs, suggesting that the relative contribution from starburst emission is generally weak in the $3\text{--}4\ \mu\text{m}$ range when compared with the continuum emission originating from an AGN. This is what we expected, as signs of the $3.3\ \mu\text{m}$ PAH emission feature are not obvious in the composite spectrum of SDSS QSOs ($=$ high-luminosity, optically selected, type 1 unobscured AGNs) (Glikman et al. 2006). Given the high fraction of PAH-undetected sources, it is difficult to impose strong constraints on starburst properties based on the upper limits of PAH strength in individual spectra. Instead, we construct a composite spectrum of PAH-undetected PG QSOs to discuss the AGN–nuclear-starburst luminosity ratios in a more quantitatively detailed manner. Among the 25 PG QSOs with not clearly detectable $3.3\ \mu\text{m}$ PAH emission in the individual spectra, we choose the 23 observed with the Subaru IRCS (i.e., we exclude I Zw 1 and 3C 273) to eliminate systematic errors caused by the inclusion of data obtained with different instruments. We normalize the flux level based on the signals in the range $\lambda_{\text{rest}} = 3.1\text{--}3.5\ \mu\text{m}$ and construct a composite spectrum in which all objects have equal weight using the IRAF task *sarith*.

Figure 4 displays the composite spectrum, in which the signature of the $3.3\ \mu\text{m}$ PAH emission is barely seen. By assuming the typical $3.3\ \mu\text{m}$ PAH profile (type A of Tokunaga et al., 1991), we estimate the $3.3\ \mu\text{m}$ PAH emission strength. The excess above the continuum is 2.1%,

and the peak wavelength is $\lambda_{\text{rest}} \sim 3.29\ \mu\text{m}$. The rest-frame $3.3\ \mu\text{m}$ PAH equivalent width is estimated to be $\sim 1\ [\text{nm}]$ (Table 2), assuming a median redshift of ~ 0.1 . The luminosity ratio of $3.3\ \mu\text{m}$ PAH emission to AGN-originated $3.35\ \mu\text{m}$ continuum (λL_{λ}) is 3.5×10^{-4} .

We here regard that the detected PAH emission toward the nuclear directions of PG QSOs is dominated by starburst activity in the true *nuclear regions*, rather than just a small fraction of spatially-extended star-forming activity, which happens to occur at the foreground of the nuclear directions, but is physically far away from the AGN nuclei, for the following reason. Our PG QSO sample is optically classified as type-1 unobscured AGNs, and so AGN obscuration is very small in the optical. Stars are formed from molecular gas, where dust usually coexists. If a large amount of star-forming activity in an extended host galaxy’s disk is present in front of the nuclear AGN direction, such a galaxy would not be classified as a type-1 AGN in the optical. Hence, the inclination of extended star-forming disks in our PG QSO sample must be biased to face-on (Wu et al. 2007), where the contamination from star-forming activity at a large physical distance from the nuclei, to the observed nuclear spectra, is minimal.

5.2. Comparison with a lower-luminosity AGN population

Figure 5 compares the $3.3\ \mu\text{m}$ PAH emission luminosity (ordinate) and the $\lambda_{\text{rest}} = 3.35\ \mu\text{m}$ continuum luminosity in λL_{λ} (abscissa) for PG QSOs. The ordinate and abscissa trace the nuclear-starburst and AGN-heated hot dust luminosities, respectively. The five PAH-detected PG QSOs are superimposed on the data points by Imanishi & Wada (2004) and Oi et al. (2010). The data point of the composite spectrum of the 23 PAH-undetected PG QSOs is also superimposed, where the median AGN continuum luminosity of $\lambda L_{\lambda}(3.35\ \mu\text{m}) \sim 3 \times 10^{44}\ [\text{ergs s}^{-1}]$ for the 23 objects is adopted in the abscissa. Figure 5 shows that (1) the data points of the PG QSOs are distributed in a higher AGN luminosity range compared with the Seyfert galaxies previously studied by Imanishi & Wada (2004) and Oi et al. (2010), and (2) the nuclear-starburst-to-AGN luminosity ratios of PG QSOs are similar to or possibly higher than those of Seyfert galaxies ($=$ lower-luminosity AGNs). The hypothesis that the nuclear-starburst-to-AGN luminosity ratio decreases with increasing AGN luminosity (Ballantyne 2008) is therefore not supported. If the apparently higher ratio in PG QSOs is real, the model developed by Kawakatu & Wada (2008) may be preferable, but more detailed discussions are difficult with our currently available dataset.

To compare Seyfert galaxies and PG QSOs, it should be noted that the AGN-heated hot dust emission luminosities for Seyferts are derived from *N*-band ($10\ \mu\text{m}$) continuum luminosities, whereas those for PG QSOs are obtained from *L*-band ($3.35\ \mu\text{m}$) continuum luminosities. The reasons for this are as follows: (1) Unlike the case for Seyfert galaxies, for which *N*-band photometric measurements with small ($< 1\text{--}2''$) apertures are available for many sources (e.g., Gorjian et al. 2004), such measurements are

not available for the observed PG QSOs. (2) Only type 1 unobscured AGNs are included in the PG QSO sample, so that dust extinction effects are not a serious concern at wavelengths shorter than the N -band. Both L - and N -band continuum luminosities trace the AGN-heated hot dust emission. However, the shorter L -band wavelength preferentially probes the hotter dust closer to the central mass-accreting SMBH at the inner part of the dusty torus compared with the longer N -band wavelength. If the solid angle of the dusty torus, viewed from the central SMBH, does not vary with the distance from the SMBH, then the L - and N -band continuum luminosities should be similar, as the luminosity ratio of the intrinsic energetic radiation of the AGN to the AGN-heated hot dust luminosity depends only on the covering factor of the dusty torus. However, if the torus is flared (Wada & Norman 2002) or warped (Sanders et al. 1989), the AGN-originated N -band-to- L -band luminosity ratio could be greater than unity. If this is the case, the true distribution of PG QSOs should move to the right relative to the current plots. Although this is a possible ambiguity, we do not expect it to be significant, as both the L - and N -band continua probe relatively hot dust ($\sim 1000\text{K}$ and $\sim 300\text{K}$, respectively) at the inner part of the dusty torus, and thus, the effects of possible torus flaring/warping should be smaller than with more widely separated wavelengths such as L -band and $>20\text{ }\mu\text{m}$ (which probes cooler dust). In fact, we compared the $3.7\text{ }\mu\text{m}$ and $10.1\text{ }\mu\text{m}$ continuum luminosities (λL_λ) measured with a $\sim 5''$ aperture for PG QSOs with available measurements of this type (Neugebauer et al. 1987; Sanders et al. 1989), but could find no evidence that the $10.1\text{ }\mu\text{m}$ continuum luminosity is systematically larger by a factor of >2 than the $3.7\text{ }\mu\text{m}$ continuum luminosity.

Finally, the bolometric luminosity of nuclear starbursts can be roughly estimated from the observed $3.3\text{ }\mu\text{m}$ PAH emission luminosity using the $3.3\text{ }\mu\text{m}$ PAH-to-infrared luminosity ratio of $\sim 10^{-3}$ for starbursts (Mouri et al. 1990; Imanishi 2002) and assuming that infrared luminosity dominates the bolometric luminosity in starbursts. To derive the AGN bolometric luminosity from the L -band continuum luminosity (λL_λ or νL_ν), we adopt a correction factor of 5 (Risaliti et al. 2010). The dotted line in Figure 5 represents the nuclear-starburst-to-AGN bolometric luminosity ratio of 0.1. Based on the assumption that starburst-driven turbulence controls the mass accretion of a central SMBH, Kawakatu & Wada (2008) argued that the nuclear-starburst-to-AGN luminosity ratio tends to increase with increasing final supermassive black hole mass (M_{SMBH}), and the ratio can be >0.1 if the mass is $>10^8 M_\odot$. Table 3 (column 4) lists the M_{SMBH} values of the observed PG QSOs, and the histogram is displayed in Figure 3(c). Four of the five PAH-detected PG QSOs (filled stars in Figure 5) with high nuclear-starburst-to-AGN luminosity ratios have $M_{\text{SMBH}} > 10^{7.8} M_\odot$. The composite spectrum of the 23 PAH-undetected PG QSOs with median $M_{\text{SMBH}} \sim 10^8 M_\odot$ has marginal PAH detection, and the implied nuclear-starburst-to-AGN luminosity ratio is ~ 0.1 . These overall observational behaviors are

reproduced by the model of Kawakatu & Wada (2008).

6. Summary

We reported the results of ground-based infrared $3\text{--}4\text{ }\mu\text{m}$ slit spectroscopy of 30 PG QSOs. The $3.3\text{ }\mu\text{m}$ PAH emission feature was used to probe the magnitude of nuclear starburst activity. The following are our primary conclusions.

1. We detected $3.3\text{ }\mu\text{m}$ PAH emission features (an effective means of probing starburst activity) in the individual spectra of five sources. For PAH-undetected PG QSOs, our composite spectrum revealed the signature of the $3.3\text{ }\mu\text{m}$ PAH emission feature. The $3.3\text{ }\mu\text{m}$ PAH-derived nuclear-starburst-to-AGN luminosity ratios were found to be comparable to, or possibly slightly higher than, those of previously investigated lower-luminosity AGNs, suggesting that AGN–nuclear starburst connections hold in the wide luminosity range of AGNs.
2. The continuum slopes Γ ($F_\lambda \propto \lambda^\Gamma$) of the PG QSOs were mostly $-1.2 \sim -0.2$, with a median value of -0.8 . This is larger (redder) than in starburst galaxies (median = -2).
3. The implied nuclear-starburst-to-AGN luminosity ratios for PG QSOs and their trend as a function of AGN luminosity could be explained by the theoretical model of Kawakatu & Wada (2008), which assumes that SMBH growth is controlled by starburst-induced turbulence.

We are grateful to Subaru and IRTF staff members for their support during our observational runs. We thank the anonymous referee for his/her useful comments. This work is based data collected at Subaru Telescope, which is operated by the National Astronomical Observatory of Japan. MI is supported by a Grant-in-Aid for Scientific Research (no. 22012006). This research made use of the SIMBAD database operated by CDS, Strasbourg, France, and the NASA/IPAC Extragalactic Database (NED), which is operated by the Jet Propulsion Laboratory, California Institute of Technology, under contract with the National Aeronautics and Space Administration.

References

- Antonucci, R. R. J. & Millar, J. S. 1985, *ApJ*, 297, 621
- Ballantyne, D. R. 2008, *ApJ*, 685, 787
- Barvainis, R. 1987, *ApJ*, 320, 537
- Baum, S. T., et al. 2010, *ApJ*, 710, 289
- Collin, S., & Zahn, J. -P. 2008, *A&A*, 477, 419
- Ferrarese, L., & Merritt, D. 2000, *ApJ*, 539, L9
- Genzel, R. et al. 1998, *ApJ*, 498, 579
- Glikman, E., Helfand, D. J., & White, R. L. 2006, *ApJ*, 640, 579
- Gorjian, V. Werner, M. W., Jarrett, T. H., Cole, D. M., & Ressler, M. E. 2004, *ApJ*, 605, 156
- Houck, J. R., et al. 2004, *ApJS*, 154, 18
- Huchra, J., & Burg, R. 1992, *ApJ*, 393, 90
- Imanishi, M. 2002, *ApJ*, 569, 44
- Imanishi, M. 2003, *ApJ*, 599, 918
- Imanishi, M., & Dudley, C. C. 2000, *ApJ*, 545, 701
- Imanishi, M., Dudley, C. C., & Maloney, P. R. 2006, *ApJ*, 637, 114
- Imanishi, M., Nakagawa, T., Shirahata, M., Ohshima, Y., & Onaka, T. 2010, *ApJ*, 721, 1233
- Imanishi, M., & Wada, K. 2004, *ApJ*, 617, 214
- Iye, M. et al., 2004, *PASJ*, 56, 381
- Kawakatu, N., Imanishi, M., & Nagao, T. 2007, *ApJ*, 661, 660
- Kawakatu, N., Umemura, M., & Mori, M. 2003, *ApJ*, 583, 85
- Kawakatu, N., & Wada, K. 2008, *ApJ*, 681, 73
- Kobayashi, N., et al. 2000, *IRCS: Infrared camera and spectrograph for the Subaru Telescope*, in *Proc. SPIE 4008: Optical and IR Telescope Instrumentation and Detectors*, eds M. Iye & A. F. Moorwood, 1056
- Magorrian, J., et al. 1998, *ApJ*, 115, 2285
- Moorwood, A. F. M. 1986, *A&A*, 166, 4
- Mouri, H., Kawara, K., Taniguchi, Y., & Nishida, M. 1990, *ApJ*, 356, L39
- Neugebauer, G., Green, R. F., Matthews, K., Schmidt, M., Soifer, B. T., & Bennett, J. 1987, *ApJS*, 63, 615
- Nishiyama, S., Nagata, T., Tamura, M., Kandori, R., Hatano, H., Sato, S., & Sugitani, K. 2008, *ApJ*, 680, 1174
- Nishiyama, S., Tamura, M., Hatano, H., Kato, D., Tanabe, T., Sugitani, K., & Nagata, T. 2009, *ApJ*, 696, 1407
- Norman, C., & Scoville, N. 1988, *ApJ*, 332, 124
- Ohsuga, K., Umemura, M., Fukue, J., & Mineshige, S. 1999, *PASJ*, 51, 345
- Oi, N., Imanishi, M., & Imase, K. 2010, *PASJ*, 62, 1509
- Peeters, E., Spoon, H. W. W., & Tielens, A. G. G. M. 2004, *ApJ*, 613, 986
- Rayner, J. T., Toomey, D. W., Onaka, P. M., Denault, A. J., Stahlberger, W. E., Vacca, W. D., Cushing, M. C., & Wang, S. 2003, *PASP*, 115, 362
- Risaliti, G., Imanishi, M., & Sani, E. 2010, *MNRAS*, 401, 197
- Roche, P. F., Aitken, D. K., Smith, C. H., & Ward, M. J., 1991, *MNRAS*, 248, 606
- Rodriguez-Ardila, A., & Viegas, S. M. 2003, *MNRAS*, 340, L33
- Sanders, D. B., Phinney, E. S., Neugebauer, G., Soifer, B. T., Matthews, K. 1989, *ApJ*, 347, 29
- Schmidt, M., & Green, R. F. 1983, *ApJ*, 269, 352
- Schweitzer, M., et al. 2006, *ApJ*, 649, 79
- Shi, Y., et al. 2007, *ApJ*, 669, 841
- Shure, M. A., Toomey, D. W., Rayner, J. T., Onaka, P., & Denault, A. J. 1994, *Proc. SPIE*, 2198, 614
- Smith, J. D., et al. 2007, *ApJ*, 656, 770
- Soifer, B. T., Neugebauer, G., Matthews, K., Egami, E., & Weinberger, A. J. 2002, *AJ*, 124, 2980
- Spinoglio, L., & Malkan, M. A. 1989, *ApJ*, 342, 83
- Tielens, A. G. G. M. 2008, *ARA&A*, 46, 289
- Tokunaga, A. T. 2000, in *Allen's Astrophysical Quantities*, ed. A. N. Cox (4th ed; Berlin: Springer), 143
- Tokunaga A. T., Sellgren K., Smith R. G., Nagata T., Sakata A., Nakada Y., 1991, *ApJ*, 380, 452
- Umemura, M., Fukue, J., & Mineshige, S. 1997, *ApJ*, 479, L97
- Umemura, M., Fukue, J., & Mineshige, S. 1998, *MNRAS*, 299, 1123
- Veilleux, S., et al. 2009, *ApJS*, 182, 628
- Voit, G. M. 1992, *MNRAS*, 258, 841
- Vollmer, B., & Beckert, T. 2003, *A&A*, 404, 21
- von Linden, S., Biermann, P. L., Duschl, W. J., Lesch, H., & Schmutzler, T., 1993, *A&A*, 280, 468
- Wada, K., & Norman, C. A. 2002, *ApJ*, 566, L21
- Wada, K., Papadopoulos, P. P., & Spaans, M. 2009, *ApJ*, 702, 63
- Watabe, Y., Kawakatu, N., & Imanishi, M. 2008, *ApJ*, 677, 895
- Watabe, Y., Kawakatu, N., Imanishi, M., & Takeuchi, T.T. 2009, *MNRAS*, 400, 1803
- Wu, X-B. 2007, *ApJ*, 657, 177
- Wu, Y., Charmandaris, V., Huang, J., Spinoglio, L., & Tommasin, S. 2009, *ApJ*, 701, 658

Table 1. Target and Observation Log

Object	Redshift	Date (UT)	Telescope Instrument	Exp (Min)	P.A. ($^{\circ}$)	Name	Standard Stars <i>L</i> -mag	Type	T_{eff} (K)
(1)	(2)	(3)	(4)	(5)	(6)	(7)	(8)	(9)	(10)
PG 0026+129	0.142	2007 January 14	Subaru IRCS	48	90	HR 145	5.1	F7V	6240
PG 0052+251	0.155	2007 January 15	Subaru IRCS	32	90	HR 217	5.2	F8V	6000
PG 0157+001 (Mrk 1014)	0.164	2003 September 8	IRTF SpeX	160	0	HR 650	4.1	F8V	6000
PG 1048+342	0.167	2007 January 14	Subaru IRCS	56	90	HR 4027	5.0	G0V	5930
PG 1202+281	0.165	2007 January 14	Subaru IRCS	24	90	HR 4496	3.5	G8V	5400
PG 1226+023 (3C 273)	0.158	2004 Apr 5	IRTF NSFCAM	28	0	HR 4708	5.0	F8V	6000
PG 1307+085	0.155	2007 January 15	Subaru IRCS	32	90	HR 4708	5.0	F8V	6000
PG 1352+183	0.158	2006 July 19	Subaru IRCS	32	90	HR 4926	5.0	F6V	6400
PG 1402+261	0.164	2006 July 19	Subaru IRCS	32	90	HR 4926	5.0	F6V	6400
PG 1613+658	0.129	2006 July 17	Subaru IRCS	24	90	HR 6360	4.5	G5V	5700
PG 0050+124 (1 Zw 1)	0.061	2003 September 8	IRTF SpeX	40	0	HR 145	5.1	F7V	6240
PG 0844+349	0.064	2007 January 14	Subaru IRCS	40	90	HR 3451	5.0	F7V	6240
PG 1001+054	0.161	2007 January 15	Subaru IRCS	40	90	HR 4079	5.3	F6V	6400
PG 1114+445	0.144	2010 April 5	Subaru IRCS	64.8	90	HR 4285	4.6	F9V	6000
PG 1115+407	0.154	2010 April 4	Subaru IRCS	64.8	90	HR 4285	4.6	F9V	6000
PG 1211+143	0.085	2007 January 15	Subaru IRCS	32	90	HR 4708	5.0	F8V	6000
PG 1229+204	0.064	2010 April 4	Subaru IRCS	28.8	90	HR 4864	4.5	G7V	5500
PG 1404+226	0.098	2010 April 5	Subaru IRCS	57.6	90	HR 5243	4.9	F6V	6400
PG 1411+442	0.089	2007 January 15	Subaru IRCS	12	90	HR 5423	4.7	G5V	5700
PG 1415+451	0.114	2010 April 5	Subaru IRCS	57.6	90	HR 5423	4.7	G5V	5700
PG 1416-129	0.129	2006 July 20	Subaru IRCS	32	90	HR 5322	4.9	F9V	6000
PG 1426+015	0.086	2010 April 4	Subaru IRCS	57.6	90	HR 5307	5.1	F7V	6240
PG 1435-067	0.129	2006 July 20	Subaru IRCS	32	90	HR 5322	4.9	F9V	6000
PG 1440+356	0.077	2010 April 5	Subaru IRCS	82.8	90	HR 5423	4.7	G5V	5700
PG 1519+226	0.137	2006 July 18	Subaru IRCS	32	90	HR 5728	4.5	G3V	5800
PG 1552+085	0.119	2010 April 4	Subaru IRCS	57.6	90	HR 5659	5.1	G5V	5700
PG 1612+261	0.131	2006 July 20	Subaru IRCS	48	90	HR 6064	5.2	G1V	5900
PG 1617+175	0.114	2006 July 17	Subaru IRCS	24	90	HR 6064	5.2	G1V	5900
PG 2130+099	0.061	2006 July 18	Subaru IRCS	24	90	HR 8077	4.6	F8V	6000
PG 2214+139	0.067	2006 July 19	Subaru IRCS	32	90	HR 8955	4.7	G0V	5930

Notes:

Col. (1): Object name. High-luminosity PG QSOs are listed in the first ten rows.

Col. (2): Redshift.

Col. (3): Observation date in UT.

Col. (4): Telescope and instrument.

Col. (5): Net on-source integration time in min.

Col. (6): Position angle of the slit. The north-south direction is defined as 0° .

Col. (7): Standard star name.

Col. (8): Adopted *L*-band magnitude of standard star.

Col. (9): Stellar spectral type of standard star.

Col. (10): Effective temperature of standard star.

Table 2. Strength of the 3.3 μm PAH Emission for Detected Sources

Object	$f_{3.3\text{PAH}}$ [$\times 10^{-14}$ ergs s $^{-1}$ cm $^{-2}$]	$L_{3.3\text{PAH}}$ [$\times 10^{41}$ ergs s $^{-1}$]	rest EW $_{3.3\text{PAH}}$ [nm]
(1)	(2)	(3)	(4)
Mrk 1014	3.0 \pm 0.2	21 \pm 1.2	7
PG 1211+143	1.7 \pm 0.5	2.7 \pm 0.8	1
PG 1411+442	1.8 \pm 0.3	3.1 \pm 0.6	2
PG 1416–129	0.66 \pm 0.2	2.5 \pm 0.7	5
PG 1440+356	2.5 \pm 0.4	3.2 \pm 0.5	2
Composite	—	—	1

Notes.

Col.(1): Object name.

Col.(2): Observed flux of 3.3 μm PAH emission in [10^{-14} ergs s $^{-1}$ cm $^{-2}$].

Col.(3): Observed luminosity of 3.3 μm PAH emission in [10^{41} ergs s $^{-1}$].

Col.(4): Rest-frame equivalent width of 3.3 μm PAH emission in [nm].

Table 3. AGN Luminosity and Continuum Slope

Object	L_L (AGN) [$\times 10^{44}$ ergs s $^{-1}$]	Continuum Slope (Γ)	M_{SMBH} [M_{\odot}]
(1)	(2)	(3)	(4)
PG 0026+129	3.9	−0.9	7.85
PG 0052+251	4.2	−1.6	8.72
PG 0157+001 (Mrk 1014)	9.1	−0.5	8.10
PG 1048+342	1.6	−0.3	8.25
PG 1202+281	4.4	+0.3	8.30
PG 1226+023 (3C 273)	63.6	−0.9	9.00
PG 1307+085	5.7	−0.8	7.86
PG 1352+183	3.2	−0.3	8.27
PG 1402+261	0.9	−0.3	7.30
PG 1613+658	2.3	−0.3	8.99
PG 0050+124 (I Zw 1)	5.7	−0.8	7.26
PG 0844+349	1.9	−1.0	7.69
PG 1001+054	7.7	−1.1	7.63
PG 1114+445	6.5	−0.3	8.41
PG 1115+407	6.6	−1.1	—
PG 1211+143	6.8	−0.4	7.88
PG 1229+204	0.9	−0.7	7.93
PG 1404+226	1.2	−0.9	—
PG 1411+442	5.2	−0.4	7.89
PG 1415+451	3.2	−0.9	7.81
PG 1416–129	1.4	−0.2	8.50
PG 1426+015	4.8	−1.0	8.75
PG 1435–067	2.8	−0.4	8.24
PG 1440+356	5.1	−0.8	7.30
PG 1519+226	2.2	−0.8	7.78
PG 1552+085	2.6	−1.1	—
PG 1612+261	1.2	−1.1	7.91
PG 1617+175	1.4	−1.2	8.70
PG 2130+099	3.2	−0.8	7.68
PG 2214+139	1.9	−0.7	8.42

Notes:

Col. (1): Object name.

Col. (2): AGN luminosity derived from continuum luminosity at $\lambda_{\text{rest}} = 3.35 \mu\text{m}$ (λL_{λ}) in 10^{44} [ergs s $^{-1}$].

Col. (3): Continuum slope Γ ($F_{\lambda} \propto \lambda^{\Gamma}$).

Col. (4): Mass of supermassive blackhole in units of solar mass, adopted from Kawakatu et al. (2007) and Watabe et al. (2009), after conversion to our cosmology. For Mrk 1014, we adopt the estimate of Watabe et al. (2009).

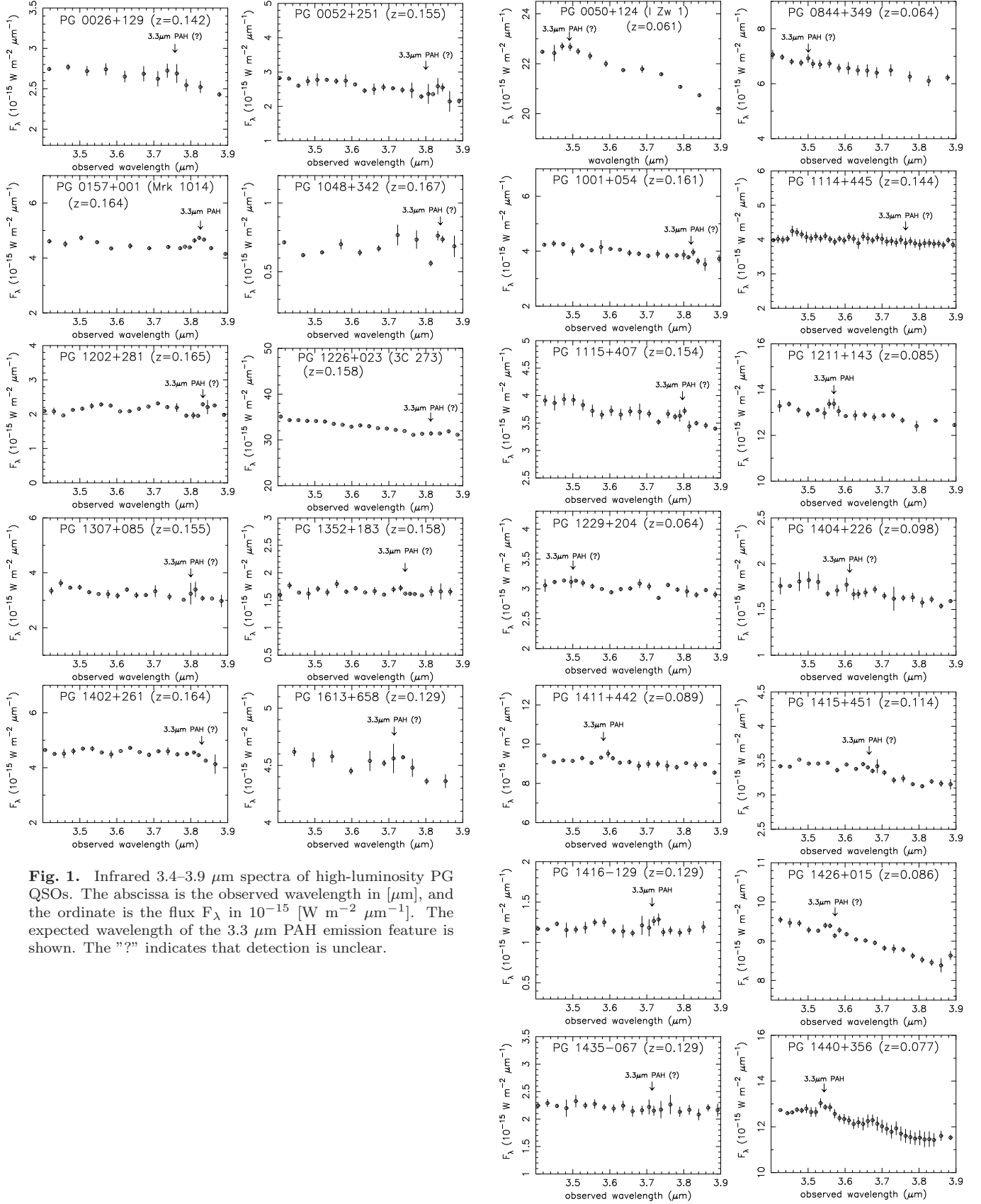


Fig. 1. Infrared 3.4–3.9 μm spectra of high-luminosity PG QSOs. The abscissa is the observed wavelength in μm , and the ordinate is the flux F_λ in $10^{-15} \text{ W m}^{-2} \mu\text{m}^{-1}$. The expected wavelength of the $3.3 \mu\text{m}$ PAH emission feature is shown. The “?” indicates that detection is unclear.

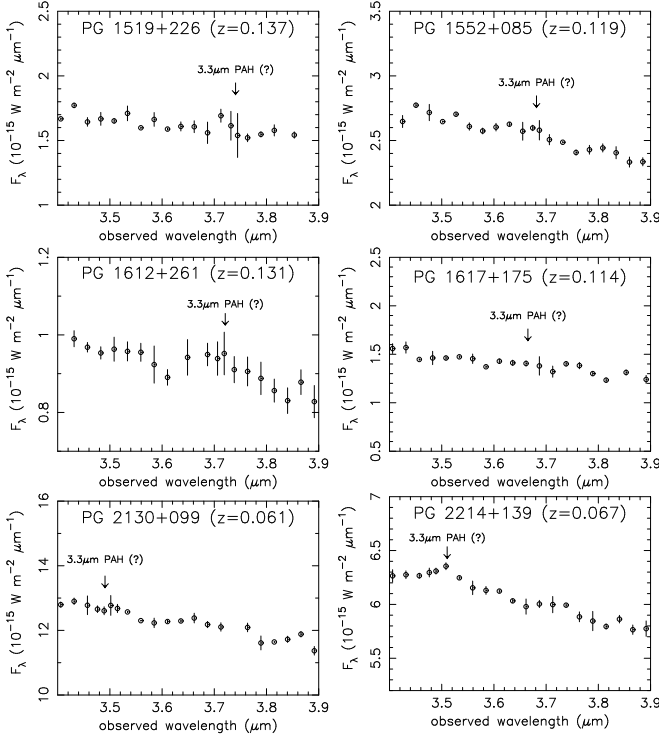


Fig. 2. Infrared 3.4–3.9 μm spectra of low-luminosity PG QSOs. Symbols are the same as in Figure 1.

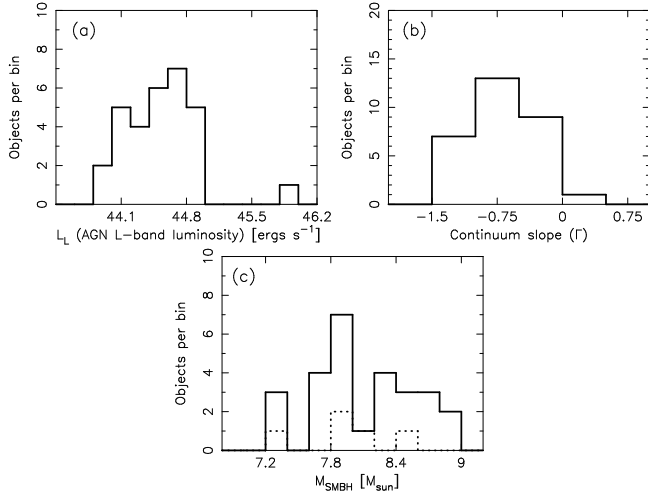


Fig. 3. (a) : Histogram of the AGN luminosities derived from continuum luminosities at $\lambda_{\text{rest}} = 3.35 \mu\text{m}$ (λL_λ) in $[\text{ergs s}^{-1}]$ for the 30 observed PG QSOs. (b) : Histogram of the continuum slopes Γ ($F_\lambda \propto \lambda^\Gamma$). (c) : Histogram of the supermassive black hole masses in units of solar mass. The solid line represents the 27 PG QSOs with available supermassive black hole masses. The dotted line represents the five PAH-detected sources.

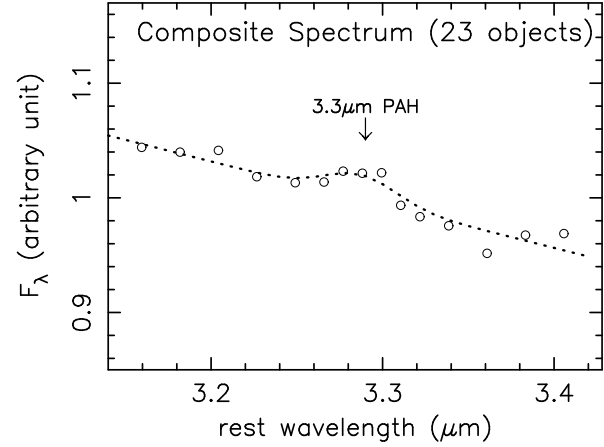


Fig. 4. Composite spectrum of the 23 PAH-undetected PG QSOs observed with the Subaru IRCS. The dotted line represents the fitted result, assuming the typical 3.3 μm PAH emission profile (§4).

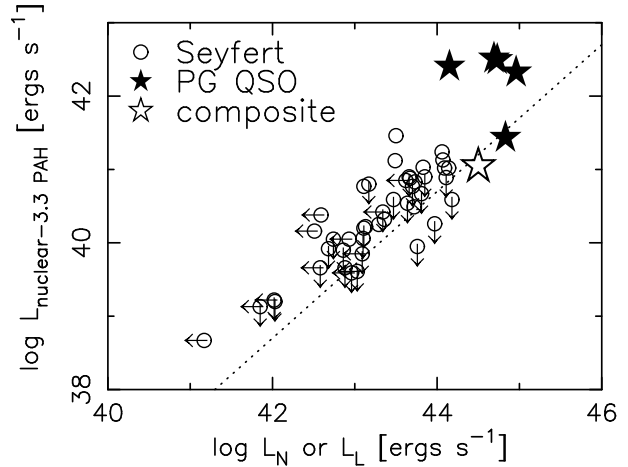


Fig. 5. The ordinate is the nuclear 3.3 μm PAH emission luminosity in $[\text{ergs s}^{-1}]$. The abscissa is the nuclear N -band (10.8 μm) luminosity (λL_λ) for Seyferts and the L -band (3.35 μm) luminosity (λL_λ) for PG QSOs in $[\text{ergs s}^{-1}]$. The ordinate and abscissa trace the nuclear-starburst and AGN-heated dust emission luminosity, respectively. Open circles represent Seyfert galaxies studied by Imanishi & Wada (2004). New results by Oi et al. (2010) are added when nuclear N -band photometric measurements are available. For the Seyfert galaxies observed in both papers, new results by Oi et al. (2010) are adopted. Filled stars represent PG QSOs with detectable 3.3 μm PAH emission in their individual spectra. The open star represents the composite spectrum of the 23 PAH-undetected PG QSOs, for which we adopt the median λL_λ (3.35 μm) value of $3 \times 10^{44} \text{ ergs s}^{-1}$ in the abscissa. The dotted line represents a nuclear-starburst-to-AGN bolometric luminosity ratio of 0.1 (see §5).